ARMY RESEARCH LABORATORY

Challenges and Development of a Multi-Scale Computational Model for Photosystem I Decoupled Energy Conversion

by Scott S. Pendley, Amy K. Manocchi, David R. Baker, James J. Sumner, Cynthia A. Lundgren, and Margaret M. Hurley

ARL-RP-445 **June 2013**

A reprint from *Applications of Molecular Modeling to Challenges in Clean Energy*; ACS Symposium Series; American Chemical Society: Washington, DC, 2013.

NOTICES

Disclaimers

The findings in this report are not to be construed as an official Department of the Army position unless so designated by other authorized documents.

Citation of manufacturer's or trade names does not constitute an official endorsement or approval of the use thereof.

Destroy this report when it is no longer needed. Do not return it to the originator.

Army Research Laboratory
Aberdeen Proving Ground, MD 21005-5069

ARL-RP-445 **June 2013**

Challenges and Development of a Multi-Scale Computational Model for Photosystem I Decoupled Energy Conversion

Scott S. Pendley, David R. Baker, and Amy K. Manocchi
Oak Ridge Institute for Science and Education

Margaret M. Hurley
Weapons and Materials Research Directorate, ARL

James J. Sumner and Cynthia A. Lundgren
Sensors and Electron Devices Directorate, ARL

A reprint from *Applications of Molecular Modeling to Challenges in Clean Energy*; ACS Symposium Series; American Chemical Society: Washington, DC, 2013.

REPORT DOCUMENTATION PAGE

Form Approved
OMB No. 0704-0188

1. REPORT DATE *(DD-MM-YYYY)*	2. REPORT TYPE	3. DATES COVERED (From - To)
June 2013	Reprint	2013

4. TITLE AND SUBTITLE
Challenges and Development of a Multi-Scale Computational Model for Photosystem I Decoupled Energy Conversion

5a. CONTRACT NUMBER

5b. GRANT NUMBER

5c. PROGRAM ELEMENT NUMBER

6. AUTHOR(S)
Scott S. Pendley,* Amy K. Manocchi,* David R. Baker,* James J. Sumner, Cynthia A. Lundgren, and Margaret M. Hurley

5d. PROJECT NUMBER

5e. TASK NUMBER

5f. WORK UNIT NUMBER

7. PERFORMING ORGANIZATION NAME(S) AND ADDRESS(ES)
U.S. Army Research Laboratory
ATTN: RDRL-WML-B
Aberdeen Proving Ground, MD 21005-5069

8. PERFORMING ORGANIZATION REPORT NUMBER
ARL-RP-445

9. SPONSORING/MONITORING AGENCY NAME(S) AND ADDRESS(ES)

10. SPONSOR/MONITOR'S ACRONYM(S)

11. SPONSOR/MONITOR'S REPORT NUMBER(S)

12. DISTRIBUTION/AVAILABILITY STATEMENT
Approved for public release; distribution is unlimited.

13. SUPPLEMENTARY NOTES
A reprint from *Applications of Molecular Modeling to Challenges in Clean Energy*; ACS Symposium Series; American Chemical Society: Washington, DC, 2013.
*Oak Ridge Institute for Science and Education, Oak Ridge, TN 37831

14. ABSTRACT
The light-harvesting and charge-transfer abilities of Photosystem I (PSI) have generated interest in the development of this system for alternative energy production and energy conversion. We describe multi-scale computational approaches that were used to study electron transfer at the PSI-biological and inorganic interfaces and to model this large protein complex. Our work in the development of an all molecular dynamics model of the PSI monomer is shown and compared to the published experimental and ONIOM optimized models with differences noted in protein and ligand structure, electron branch characterization, and ionization and orbital potentials in the P700 chlorophylls. Differences between the docking of cytochrome c_6 and plastocyanin to PSI using established docking algorithms and molecular dynamics are described. Finally, dipole calculations, luminal surface hydropathicity and polarity characterization were used to predict improvements in surface-assembled monolayer design.

15. SUBJECT TERMS
photosystem I, cytochrome c_6, computational chemistry, molecular modeling, docking, quantum mechanics, self-assembled monolayer, photoelectrochemistry, electron transfer, hydrogen production, molecular mechanics, computational chemistry

16. SECURITY CLASSIFICATION OF:			17. LIMITATION OF ABSTRACT	18. NUMBER OF PAGES	19a. NAME OF RESPONSIBLE PERSON
a. REPORT	b. ABSTRACT	c. THIS PAGE			Margaret M. Hurley
Unclassified	Unclassified	Unclassified	UU	32	19b. TELEPHONE NUMBER (*Include area code*) 410-306-0728

Chapter 10

Challenges and Development of a Multi-Scale Computational Model for Photosystem I Decoupled Energy Conversion

Scott S. Pendley,[1] Amy K. Manocchi,[2] David R. Baker,[2] James J. Sumner,[2] Cynthia A. Lundgren,[2] and Margaret M. Hurley*,[1]

[1]Weapons and Materials Research Directorate, United States Army Research Laboratory, Aberdeen Proving Ground, Maryland 21005
[2]Sensors and Electron Devices Directorate, United States Army Research Laboratory, Adelphi, Maryland 20783
***E-mail: margaret.m.hurley12.civ@mail.mil**

The light-harvesting and charge-transfer abilities of Photosystem I (PSI) have generated interest in the development of this system for alternative energy production and energy conversion. We describe multi-scale computational approaches that were used to study electron transfer at the PSI-biological and inorganic interfaces and to model this large protein complex. Our work in the development of an all molecular dynamics model of the PSI monomer is shown and compared to the published experimental and ONIOM optimized models with differences noted in protein and ligand structure, electron branch characterization, and ionization and orbital potentials in the P700 chlorophylls. Differences between the docking of cytochrome c_6 and plastocyanin to PSI using established docking algorithms and molecular dynamics are described. Finally, dipole calculations, luminal surface hydropathicity and polarity characterization were used to predict improvements in surface-assembled monolayer design.

Keywords: Photosystem I; cytochrome c_6; computational chemistry; molecular modeling; docking; quantum mechanics; self-assembled monolayer; photoelectrochemistry; electron transfer

In Applications of Molecular Modeling to Challenges in Clean Energy; Fitzgerald, G., et al.; ACS Symposium Series; American Chemical Society: Washington, DC, 2013.

Introduction

Oxygenic photosynthesis provides the energy source, directly or indirectly, for all complex, multi-cellular organisms on Earth. This biological process couples the energy derived from photo-excitation to split water and reduce CO_2 in order to create complex carbohydrates in plants, algae, and cyanobacteria. Two large transmembrane protein complexes, photosystems (PS) I and II, are instrumental in the first steps involved in charge separation and the resulting translocation of electrons across the thylakoid membrane. The first step of the light-driven reactions in photosynthesis occurs in PSII, where light energy is harnessed by the chlorophylls within PSII, followed by the oxidation of water to produce protons, oxygen gas, and electrons. The electrons produced in this reaction are quickly transferred through a chain of cofactors and carriers (including plastoquinones, plastocyanin, and cytochromes) to the other light harvesting complex, PSI. Depending upon the organism, PSI receives the transferred electrons from either plastocyanin or cytochrome c_6 at the P700 chlorophylls on its luminal side and rapidly transports the electrons to the terminal iron-sulfur cluster, FB, at its stromal side. There the electrons are used to reduce NADP+ to NADPH in the ferrodoxin-NADP+ oxidoreductase complex. The transmembrane potential created from the electron transport through the two photosystems and the proton concentration gradient is further used to drive ATP synthesis and other cellular processes.

PSI has become popular in the solar energy conversion literature recently because of its light harvesting ability and charge transfer properties. Most importantly, PSI is able to transport electrons across the thylakoid membrane with an internal quantum efficiency near unity (*1*). Although the comparison of energy conversion efficiency among disparate processes is not not straightforward (*2*), the harnessing and enhancement of natural photosynthetic processes is of great interest, and the integration of PSI into chemical or electrical systems for the conversion of light energy to chemical energy has been pursued for several decades. These efforts were initially focused on the optimization of H_2 production in algae (*3–6*) through metabolic (*7–9*) and later genetic controls (*8*, *10*). More recent work has focused on decoupling photosynthesis by crosslinking PSI with hydrogenases (*11–16*) or metal complexes (*17*, *18*) in order to direct electron flow to drive hydrogen evolution. Despite this increased interest in PSI, the fundamental understanding of the dynamic docking of transfer proteins to PSI, as well interactions between PSI and non-native environments is lacking. This work focuses on elucidating the fundamental interactions between PSI and its surrounding non-native environment in order to improve the integration of PSI into energy generating devices.

Computational analysis of proteins and their interaction with surrounding environments is highly valuable in predicting the dynamic behavior of these complex biological systems. Interest in Photosystem I in particular has increased dramatically with the release of the 2.5 Å resolution cyanobacterial PSI structure in 2001 (*19*). The extremely large size of the protein complex, approximately one megadalton for the cyanobacterial trimer, makes computational characterization highly challenging. Much of the earlier work used the published structure to

In Applications of Molecular Modeling to Challenges in Clean Energy; Fitzgerald, G., et al.;
ACS Symposium Series; American Chemical Society: Washington, DC, 2013.

develop models of spectral properties and energy transfer kinetics (*20–22*). Ivashin et al. optimized select ligands (α-chlorophyll *a*, phylloqionones) and residues at the B3LYP/6-31G* level in combination with ZINDO/S level electronic coupling calculations to study differences between the A- and B-branches of the electron transfer chain in PSI (*23*). Much attention has also been paid to the advanced treatment of electrostatics in this system (*24–26*). The P700 site has been studied with TDDFT (*24*, *27*) and semiempirical methods (*28*). Lin and O'Malley used a two layer (B3LYP/6-31G(d):UFF) ONIOM methodology to optimize models of the phyllosemiqionone free radical in the A_{1A} and A_{1B} sites (*29*). Canfield et al. utilized the ONIOM methodology to systematically partition and optimize the entire protein in a sequential fashion (*30*). This optimized structure was then used for a variety of analyses (*31*). Attempts to dock PSI are less numerous in the literature. Myshkin et al. used a variety of standard docking algorithms to model the plastocyanin/PSI complex (*32*). Jollet et al. used a specialized algorithm to dock the PsaC subunit onto PsaA/PsaB (*33*).

The computational approaches in this study are focused on understanding the interactions between PSI and its charge carrier proteins or surrounding non-native environment in order to develop improved coupling (and electron transport) between biological components (cytochrome c_6/PSI and also between PSI and physical components of electrochemical devices). Simulations at multiple scales were used to address these challenges. Modeling approaches included docking, all-atom molecular dynamics (MD), and quantum mechanics (QM) using density functional theory (DFT). Development of coarse grained models when system size and sampling time scales exceed the current limits of all-atom MD are also underway and will be reported elsewhere. Here we detail initial findings for this ongoing project which is the first to report PSI dynamics and extend multiscale modeling of the PSI complex past the QM/MM level.

Modeling the PSI Complex

In cyanobacteria, photosystem I exists as a clover-shaped trimer embedded in the lipid bilayer of the thylakoid membrane. Each monomer is composed of 12 protein chains, 96 chlorophylls, 22 carotenoids (β-carotene), 2 phyloquinones, 3 iron-sulfur clusters, 4 unique lipid molecules, and a multimer-coordinating calcium ion (*19*). Nine of the protein subunits feature transmembrane domains while subunits PsaC, PsaD, and PsaE compose the stromal hump. The interface of the two largest subunits, PsaA and PsaB, creates a pseudo C_2 axis at the center of the PSI monomer complex with pigment and lipid cofactors arranged in two branches along the axis (*19*). β-carotene, the lipids (1,2-dipalmitoyl-phosphatidyl-glycerole and 1,2-distearoyl-monogalactosyl-diglyceride), and most of the axial chlorophylls make direct contact with PsaA and PsaB (*19*). Protein chains PsaJ, PsaK, PsaL, PsaM and PsaX coordinate antennae α-chlorophyll *a* molecules directly or through bridging solvent contacts (*19*). Stabilizing hydrophobic contacts with the carrotenoids are made by amino acid residues in chains PsaF, PsaI, PsaJ, PsaL, PsaM, and PsaK (*19*). PsaF has also been proposed to coordinate docking of

In Applications of Molecular Modeling to Challenges in Clean Energy; Fitzgerald, G., et al.;
ACS Symposium Series; American Chemical Society: Washington, DC, 2013.

plastocyanin and cytochrome c_6 to the P700 domain found at the center of the C_2 axis (*34*). In cyanobacteria, this protein chain is significantly truncated compared to its plant complement (*19*) and interaction may be limited due to its relatively distal location. A graphical representation of the PSI monomer from both the side and stromal views is shown in Figures 1a and 1b.

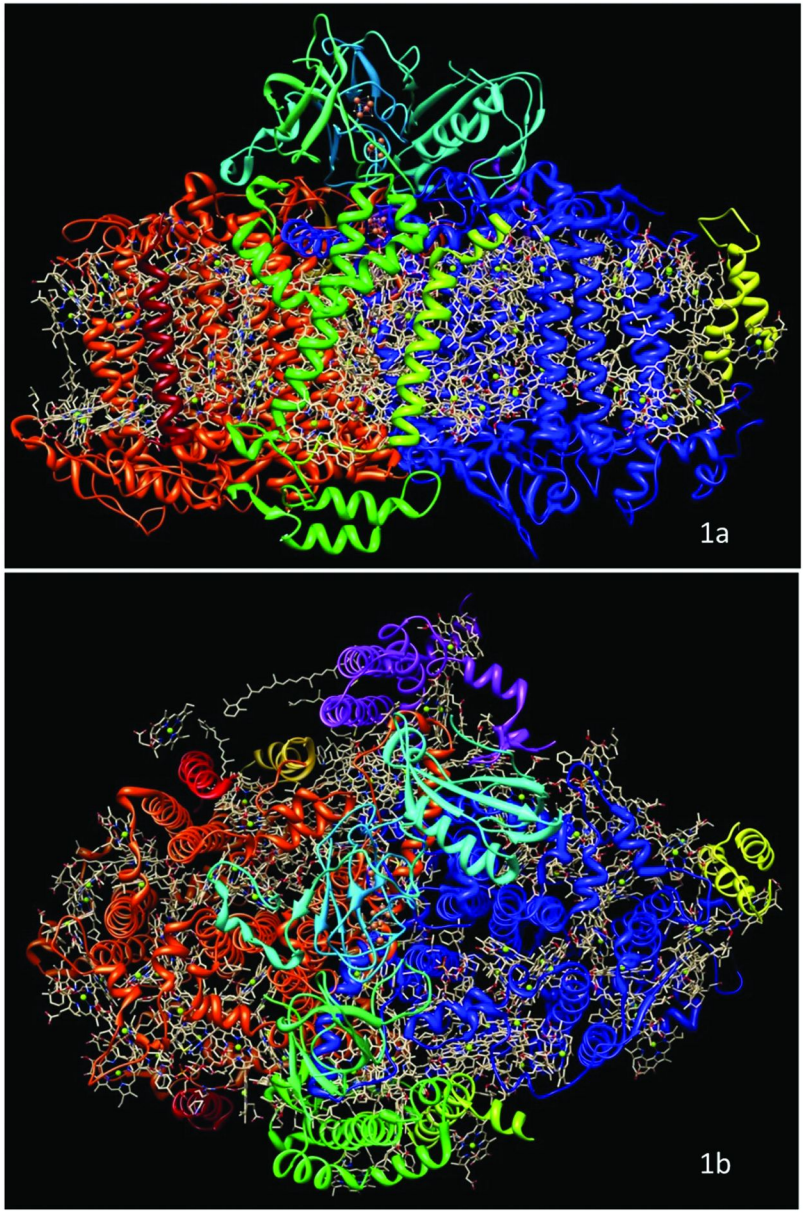

Figure 1. Ribbon representation of cyanobacterial PSI (PDB ID: 1JB0) from side (1a) and stromal views (1b). Coloring was chosen to differentiate the protein chains that compose the complex and emphasize the C_2 axis.

In Applications of Molecular Modeling to Challenges in Clean Energy; Fitzgerald, G., et al.;
ACS Symposium Series; American Chemical Society: Washington, DC, 2013.

Initial PSI Molecular Dynamics (MD) Model

An all-atom molecular model of PSI was built using the high resolution crystal structure (2.5 Å resolution) of Photosystem I from cyanobacteria (*19*) (PDB ID: 1JB0) as the initial starting trajectory. Some modifications to the structure were necessary and included: splitting the PsaA chain between residues 262 and 266 due to missing residues, inserting an alanine residue into position 33 of the PsaK chain, splitting the PsaK chain between residues 43 and 55 due to missing residues, and removal of native waters and calcium ion from the model structure. Ligand parameters and atomic charges were determined using the R.E.D. vIII (*35*) and antechamber (*36*) programs. Parameterization of the iron-sulfur (4Fe4S) clusters assumed an oxidized state and atomic charges were calculated using a tetra-coordinated methyl sulfide capping groups whose group atomic charges were constrained to zero, similar to work performed by Torres et al. (*37*). RESP (restrained electrostatic potential) derived atomic charges (*38*) based on QM calculations were determined consistent with the AMBER ff99SBildn/GAFF (*39*) force fields using the HF-6/31G* basis set for all ligands with the exception of the iron-sulfur cluster. Due to the known limitations of the Hartree-Fock basis sets to model metal centers, the 4Fe4S structure was optimized and molecular electrostatic potential (MEP) calculated using the DFT BVP86/cc-pVDZ basis set. The all-atom molecular dynamics simulation was performed using the AMBER ff99SBildn force field (*40*) with adjustments to the phi and psi amino acids dihedrals consistent with the Robert Best parameter set (*41*). The protein complex was solvated using a surrounding octahedron shell of explicit TIP3P waters which extended at least 12 angstroms from the structure in all directions. Explicit salt ions using the Cheatham and Joung parameter set (*42*) were used to neutralize the system. Periodic boundary conditions were applied using the particle mesh Ewald method approach with a small (1 fs) time step to ensure stability in the large complex. Minimization was performed in two stages, allowing for initial solvent minimization in the presence of restrained solute molecules and later unrestrained system minimization. Equilibration, similiarly, used three stages with weak solute restraints during a slow heating stage to the final temperature of 300K followed by 500 ps of unrestrained equilibration to remove any hot spots in the simulation prior to production MD.

During the first 3 ns of all-atom MD of the PSI complex, the all-atom RMSD consistently increased from the starting trajectory (Figure 2). Comparing the final snapshot at 3 ns to published structure, significant loss of secondary structure can be seen originating in the PsaC domain (Figure 2). Using scanning RMSD (*43*) to measure local fluctuations on the time course of the simulation, the majority of large motions found in and near PsaC occurred proximal to the F_B iron-sulfur cluster. At this region many of the stabilizing salt bridges and hydrogen bonds between PsaC and nearby PsaD and PsaE chains are formed. The large atomic charges assigned to the iron-sulfur clusters create competitive electrostatic interactions at the protein tertiary domains which disrupt neighboring salt bridges and eventually lead to structure deformation. After the results from the QM atomic charge fitting were re-evaluated, it was determined that the molecular electrostatic potential for the iron-sulfur clusters was further distributed along

In Applications of Molecular Modeling to Challenges in Clean Energy; Fitzgerald, G., et al.;
ACS Symposium Series; American Chemical Society: Washington, DC, 2013.

attached thiol ligands and that the charge constraints resulted in artificially large charges to the iron-sulfur molecules. Variance between ligand-complex fit and complex-alone fit atomic charges confirm the need to include 4Fe4S bound amino acids in the charge assignment protocol. While developing improved 4Fe4S parameters, a second model of the PSI complex lacking the stromal hump (PsaC, PsaD, PsaE protein chains and the iron-sulfur clusters) was constructed to complete simulations focused on dynamic structural fluctuations in the lower portion of the electron transfer chain and interactions of external moieties (e.g. transfer proteins and SAMs) with the luminal surface.

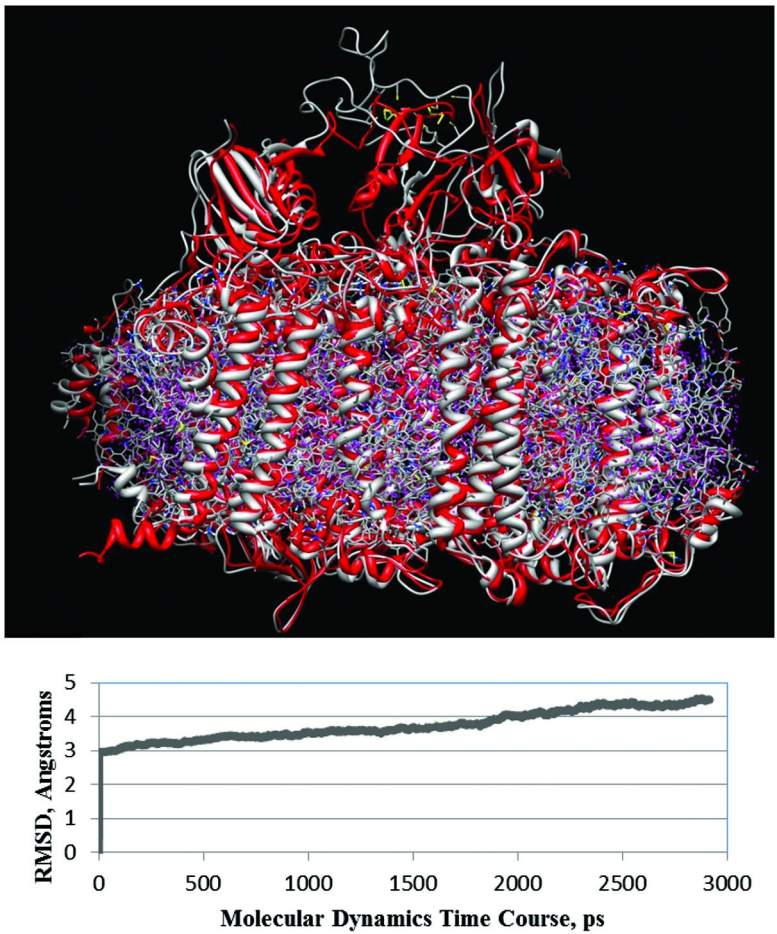

Figure 2. Variance of the initial MD model from the published structure shows deformation in the PsaC chain. In the ribbon diagram (top) the published structure is shown in red, while the MD model is shown in white. On the bottom, all-atom RMSD of initial MD model from PSI X-ray structure is shown over the simulation time course.

In Applications of Molecular Modeling to Challenges in Clean Energy; Fitzgerald, G., et al.;
ACS Symposium Series; American Chemical Society: Washington, DC, 2013.

PSI MD Model Lacking a Stromal Hump

The design of a PSI model lacking a stromal hump followed the approach described above. A one-dimension all-atom RMSD plot from the published structure through the 68 ns time course can be seen in Figure 3.

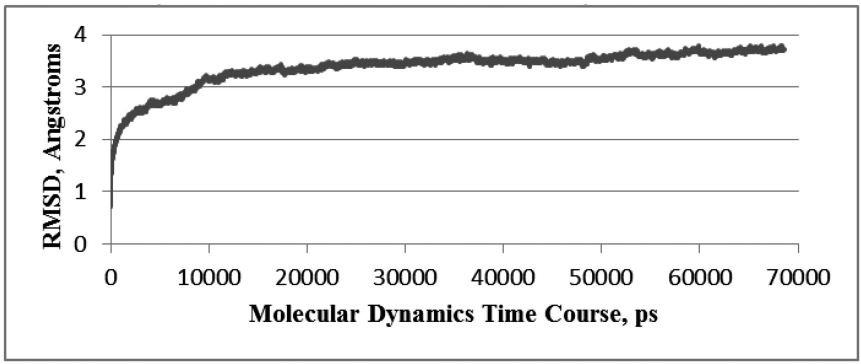

Figure 3. All-atom RMSD of MD model (lacking stromal hump) from PSI X-ray structure.

Several differences between the computational model and published structure are observed in the ligand interactions, the electron transport paths, and at the solvent interface. In general, the MD model is a more compressed system than the X-ray structure showing constriction of solvent-exposed hydrophobic surfaces in both protein and ligand molecules. Several of the most visible changes are found among the antennae α-chlorophyll *a* molecules. Of these, CL1 1601 (a chlorophyll in the M chain) shows the greatest movement among the chlorophylls at 13 Å from its initial, isolated position to close proximity with a neighboring chlorophyll, CL1 1201 (see Figure 4). Similar movements are seen with chlorophylls CL1 1217 and 1302. CL1 1217 moves 6 Å from a staggered position with CL1 1209 to bridge CL1 1209 and CL1 1218 (Figure 4). CL1 1302 moves 8.3 Å to improve contacts with neighboring pigments. The energetic driving forces for other chlorophyll movements are less clear: for example, CL1 1303 moves 7 Å without visible improvement in local interactions with antennae chlorophyll neighbors. The published structure of the PSI complex lacks many coordinates for atoms associated with the chlorophyll hydrocarbon tails and many of these positions were built at the time of model generation based on a fairly simplistic energy minimizer. It is plausible that the 80 ns time frame of this MD simulation may not be sufficient to allow for optimal packing or refolding of those regions and this may contribute to some of the differences seen.

In Applications of Molecular Modeling to Challenges in Clean Energy; Fitzgerald, G., et al.;
ACS Symposium Series; American Chemical Society: Washington, DC, 2013.

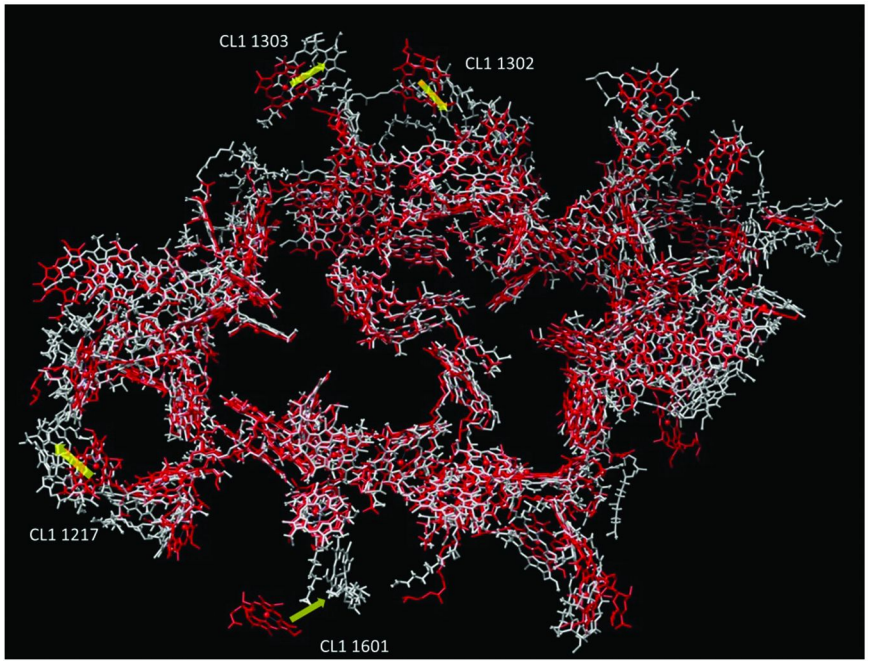

Figure 4. Localization of chlorophyll molecucles in X-ray (red) and molecular dynamics (white) structures.

In Figure 5, a side view ribbon representation of both crystal and MD models of PSI is shown. Differences in protein positions can be observed with the emphasis on the PsaL chain which is shown in dark grey. The movement of solvent-exposed helices from solution to the transmembrane region is fairly consistent with structural motions in the MD model. The crystallization of photosystem I was accomplished using β-dodecylmaltoside as a detergent for the lipoprotein complex. Detergents and surfactants can minimize hydrophobic forces in protein molecules which may account many of the differences seen at the solvent interface. Furthermore, some uncharacteristically fast motions in the solvent-exposed peptide transmembrane helices are seen in the MD model which suggests that future simulations which lack detergent (such as ours) should include additional bilayer lipid molecules beyond those defined in the X-ray structure to maintain ideal, native structure.

In Applications of Molecular Modeling to Challenges in Clean Energy; Fitzgerald, G., et al.;
ACS Symposium Series; American Chemical Society: Washington, DC, 2013.

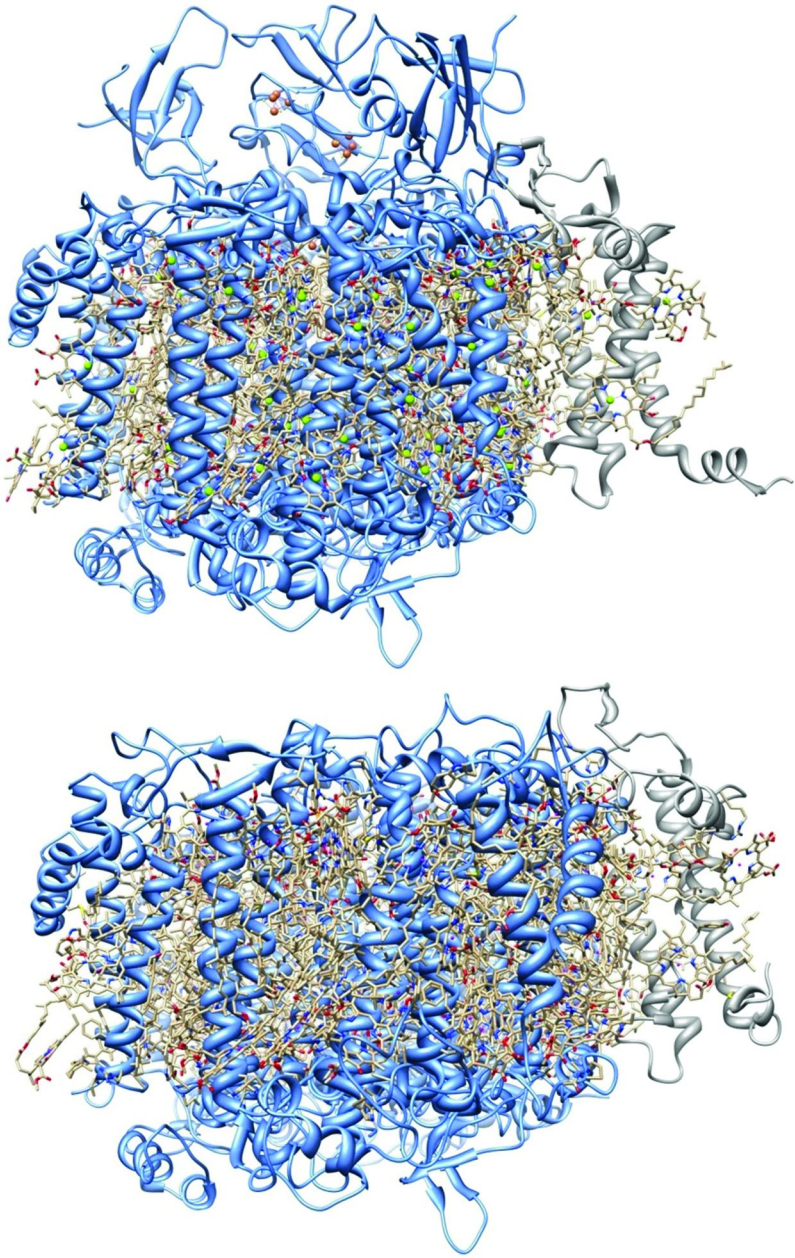

Figure 5. Structural differences between the PSI X-ray structure (top) and the MD model (bottom).

In Applications of Molecular Modeling to Challenges in Clean Energy; Fitzgerald, G., et al.;
ACS Symposium Series; American Chemical Society: Washington, DC, 2013.

Electron transfer through the core of PSI takes places through one of two electron transfer pathways; branch A or branch B (*44*). These branches begin at the luminal pair of chlorophyll molecules that are designated the P700 site based on the absorbance maxima at 700 nm (*1*). From here, the branches diverge to separate chlorophyll molecules with decreasing redox potentials. Along the A branch, electron flow proceeds from the P700 chlorophylls to A_{-1A} (an α-chlorophyll *a* molecule), A_{0A} (another α-chlorophyll *a* molecule), A_{1A} (a phyloquinone molecule), to F_X, F_A, and F_B which are 4Fe4S iron-sulfur clusters (*23*). The B branch uses similar intermediates: A_{-1B} (an α-chlorophyll *a* molecule), A_{0B} (an α-chlorophyll *a* molecule), A_{1B} (a phyloquinone molecule), and convergence with the A branch on the use of F_X, F_A, and $F_{B(23)}$. Electron transfer rates through the respective branches are species specific and are often a function of distances between intermediates in the branch. In *Synechococcus elongatus*, a 10 fold increase in electron transfer rate (*44–46*) is seen in the B branch compared to the A branch. A variety of factors have been investigated to determine their role in this behavior, including the contribution of surrounding residues on the midpoint potential of phylloquinones A_{1A} and A_{1B} (*24*, *47*), as well as a B branch specific inclusion of a tryptophan residue (TRP B673) which may act as an electron acceptor between A_{1B} and the F_x iron-sulfur cluster (*19*, *23*). Some preliminary measurements of the chlorophyll and phylloquinone distances along the A and B branches were made to compare against the published structure (see Table I).

Table I. Measured Distances between Electron Carriers in the PSI X-ray and MD Structures

Measured Distance	*X-ray Structure*	*MD model*
P700 chlorophylls	6.34 Å	5.80 Å
$P700_A$ to A_{-1A}	11.72 Å	12.74 Å
A_{-1A} to A_{0A}	8.13 Å	8.74 Å
A_{0A} to A_{1A}	8.78 Å	9.89 Å
$P700_B$ to A_{-1B}	11.95 Å	12.62 Å
A_{-1B} to A_{0B}	8.22 Å	7.60 Å
A_{0B} to A_{1B}	8.78 Å	9.37 Å
$P700_B$ to A_{1A}	26.0 Å	26.2 Å

While the molecular coordinates in the interior of PSI complex are very similar between the MD model and X-ray structure, some changes are notable. In the computational model, an increase is seen in the distance between the P700 chlorophylls and the first set of chlorophyll intermediates, as well as the distance between the second pair of chlorophyll and the phylloquinone intermediates. The distances between the magnesium ions of the P700 chlorophyll pair has decreased

In Applications of Molecular Modeling to Challenges in Clean Energy; Fitzgerald, G., et al.;
ACS Symposium Series; American Chemical Society: Washington, DC, 2013.

by a half angstrom, although the chlorophyll ring distance itself is relatively unchanged (Figure 6 and next section). The distance between the B branch P700 chlorophyll and the A branch phylloquinone has increased slightly compared to the published structure and the experimental value of 25.4 Angstroms obtained from spin-echo modulation experiments (*48*). In the X-ray structure the distances between electron intermediates is smallest in the A branch while in the MD model, smaller distances are found in B branch which may contribute to the differences seen in the electron transfer rates.

Preliminary PSI Quantum Mechanical (QM) Model

Theoretical studies of α-chlorophyll *a* and similar porphyrins have been a topic of interest for decades due to their critical involvement in photosynthesis. Numerous TDDFT (time dependent density functional theory) studies of the single α-chlorophyll *a* (Chl a) molecule exist, which were able to reproduce experimental adsorption energies with varying success (*49*, *50*).

The P700 site in photosystem I is a dimer made of Chl a and Chl a′ (the C10 epimer of Chl a). Computational analysis of the P700 dimer has also been performed. It is interesting to note that a variety of P700 models have been studied. The molecular orbital analysis of Plato et al. (*28*), which was performed at the RHF-INDO level, started from the experimental X-ray crystal structure and expanded to a series of models of varying sophistication, although no complete geometry optimization of the P700 site was attempted. This work demonstrated the effect of the interactions of the chlorophyll with the protein environment, in particular Thr A743, His A860, and His B660, which they postulated to be implicitly involved in the development of spin and charge asymmetry within the P700 dimer. Sun et al. (*27*) utilized TDDFT on an optimized model of P700 obtained from the crystal structure and found its excitation to be "intrinsically asymmetric" without the inclusion of neighboring residues. Saito and Ishikita (*51*) used QM/MM to study the cationic state and spin distribution of the P700 site, keeping the coordinates of the MM region fixed to the crystal structure.

Gunner (*52*) noted the importance of accounting for the normal thermal motions of photosynthetic proteins and their subtle but far-reaching effects on redox potential and other important properties. Dreuw et al. (*53*) stressed the importance of quantum mechanical optimization from the experimental crystal structure when studying excited states of pigment-protein complexes. The most complete structural optimization of PSI was generated by Canfield et al. (*30*). However, this work utilized the ONIOM model and optimized sections of the complex in a sequential fashion. We are unaware of any studies of the P700 site, or indeed any portion of the PSI electron transfer chain, starting from a classically thermalized structure of the PSI complex.

The current work attempts to address this. What follows is a preliminary assessment of the physical and electronic structure of a model P700 dimer derived from a 2 ns averaged structure of the PSI MD model described in the previous section. Results are compared to similar data derived from the experimental X-ray crystal structure (1JB0), and to the optimized structure of Canfield et al. Quantum calculations are performed at the B3LYP/6-31G(d,p) level of both the neutral and

In Applications of Molecular Modeling to Challenges in Clean Energy; Fitzgerald, G., et al.;
ACS Symposium Series; American Chemical Society: Washington, DC, 2013.

charged (+1) P700 complex. For ease of computation in the single point quantum runs only, the phytyl ester of both Chl a and Chl a′ has been replaced with a methyl ester, as is common in the literature (*54*). Differences between the thermalized P700 structure and the original crystal structure are moderate and can be seen in Figure 6.

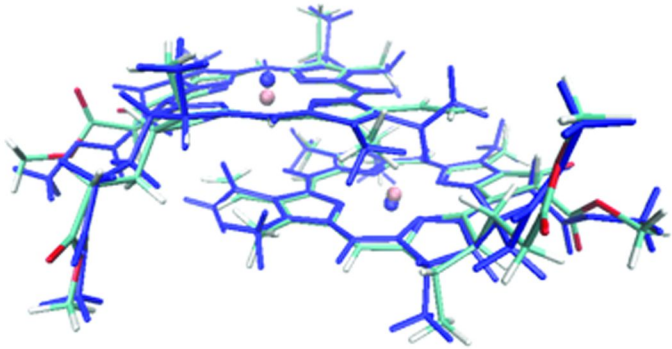

Figure 6. Overlay of thermalized P700 structure (standard coloring by element) and X-ray crystal structure (shown in blue).

The heavy-atom RMSD of our structure with respect to the X-ray structure is 0.61 angstroms. There is obvious fluctuation in sidechains, as expected, and some variation in twisting of the 5 membered moities of the chlorin ring. The most prominent difference is a marked movement in plane of the chlorin central magnesium atoms. The Canfield structure (not shown) has a heavy-atom RMSD of 0.29 angstroms with respect to the crystal structure, also due to sidechain fluctuation and some chlorin ring twisting. The central magnesiums atoms in this instance remain slightly out of plane. In all cases the average interplanar distance between the chlorin rings remains close to the published value of 3.6 angstroms (*19*).

Ionization potentials are calculated from the electronic energy in the neutral and cationic states. For all three models, the calculated IP is within the range for variations in the chlorophyll dimer P680 in photosystem II calculated at the B3LYP/6-31G(d) level by Takahashi et al. (*55*).

The role of His A680 and B660 has been discussed at length within the literature (*28*, *56*, *57*). Within the crystal structure 1JB0 it is apparent that these residues are ligands of the P700 Mg atoms, as shown by the short HisN-Mg distances given in Table II. Canfield et al. chose to honor this bonding pattern and protonate at the delta position (*30*), while in the current model these residues are protonated at the epsilon position. Loss of this explicit ligand may in part account for the relaxation of the magnesium ions back into the plane of the chlorin rings, as well as the larger HisN-Mg distance in the current model relative to the crystal structure and Canfield structure. This point is of great computational interest, as previous studies have argued that complexation of the chlorin with the central magnesium leads to the destabilization of the chlorophyll *a* HOMO and LUMO+1,

In Applications of Molecular Modeling to Challenges in Clean Energy; Fitzgerald, G., et al.;
ACS Symposium Series; American Chemical Society: Washington, DC, 2013.

with little effect on the HOMO-1 or LUMO, leading to a slight change in the HOMO/LUMO gap (*49*, *58*). While the frontier orbitals of the current model do differ from the 1JB0 and Canfield models, the stated HOMO/LUMO trend is not followed, and therefore the effect of Mg complexation, while undeniably important, has been lost in the other effects from thermalizing the protein complex. It must be pointed out, however, that the calculated HOMO-LUMO gaps of the three models are in very reasonable agreement both with each other and with previously published values. HOMO-1 and LUMO+1 values are not provided for the current model, but differ only slightly from the HOMO and LUMO values, as has frequently been noted within the literature for Chl a and similar systems (*59*).

Table II. Physical and Electronic Structure Properties of Three P700 Models at B3LYP/6-31G(d,p)

	Current Work	*1JB0*	*Canfield*
IP (eV)	6.01	5.78	5.78
Frontier Orbital energy HOMO (eV)	-5.11	-4.88	-4.89
Frontier Orbital Energy LUMO (eV)	-2.91	-2.57	-2.7
HOMO-LUMO eV	2.19	2.31	2.19
Mg-Mg distance (angstroms)	5.8	6.34	6.26
HisN-Mg distance (angstroms)	3.99/4.49	2.36/2.26	2.20/2.22
Heavy-Atom RMSD wrt 1JB0 (angstroms)	0.61	0	0.29

A variety of additional measurable properties are intimately related to the geometric and electronic structure of the cyanobacterial P700 moiety (in both its singlet and triplet form), as well as for additional sites within the electron transfer chain. Methods used have included FTIR (*60–62*), as well as EPR and ENDOR techniques (*28*, *63*, *64*), and some quantum chemical analysis has been performed. Work evaluating our thermalized model within the context of this data is underway.

Biological Interactions with PSI

In cyanobacteria, electron transfer to PSI occurs through the intermediate of charge carrier proteins, plastocyanin or cytochrome c_6. In order to efficiently couple the charge carrier protein, cytochrome c_6 in this case, to PSI outside of its natural environment, a detailed fundamental understanding of this dynamic protein-protein docking event is vital. Significant prior research focused on the binding of plastocyanin and cytochrome c_6 to PSI has been published and while

In Applications of Molecular Modeling to Challenges in Clean Energy; Fitzgerald, G., et al.;
ACS Symposium Series; American Chemical Society: Washington, DC, 2013.

the conformation and orientation of the plastocyanin-PSI complex has been well elucidated, the cytochrome c_6 docking structure is still unknown. Ford et al. were able to characterize the binding site of plastocyanin to PSI in vascular plants using Fourier difference analysis of arrays of PSI located on the chloroplast granula (*65*). They propose that plastocyanin binds close to the center of PSI complex between the PsaA and PsaB domains with a slight bias towards the PsaL subunit of the complex (*65*). In this binding pocket, two solvent-exposed, hydrophobic tryptophan residues may form an important feature of the ligand recognition site (*66*). While no structures of cytochrome c_6 bound to PSI have been resolved or published in the scientific literature, cytochrome c_6 has been proposed to bind to PSI in a similar manner as plastocyanin. Plastocyanin and cytochrome c_6 share many attributes which suggest a common docking orientation including similar hydrophobic faces that match the docking surface of PSI (*67*), similar response to docking site mutations (*68*), and similar increases in affinity when positive mutations are introduced to increase the electrostatic attraction between the proteins and PSI (*68*).

Initial efforts to determine the cytochrome c_6-PSI binding site followed the efforts of Myshkin et al. (*32*) by using established docking algorithms to compare the plastocyanin and cytochrome c_6 predicted docking complexes. Molecular structures used in docking (and later all-MD simulation) were taken from RCSB Protein Data Bank and include the crystal structure of Photosystem I from *Synechococcus elongatus* (PDB ID: 1JB0) (*19*), an NMR structure of reduced plastocyanin from *Synechocystic* sp. PCC 6803 (PDB ID: 1JXD) (*69*), and the NMR solution structure of cytochrome c_6 from *Synechococcus elongatus* (PDB ID: 1C6S) (*70*). Due to the limitations of the docking software, only protein components were used. Docked complex structures from the HADDOCK (*71*), CLUSPRO (*72*), GRAMM-X (*73*), and RosettaDOCK (*74*) servers emphasized a noncannonical, unlikely transmembrane localization of the electron carriers with respect to PSI. Refinement of both plastocyanin and cytochrome c_6 docking to the luminal surface of PSI followed using a Python based interface to the Rosetta docking program (*75*). These docking simulations implemented a 3 angstrom translation and 8 degree rotation angle of the ligand molecules, followed by a subsequent alignment of the molecules to explore the PSI surface. 4000 docking configurations were tested and the docking energy predicted by the Rosetta algorithm was calculated for each structure. This Rosetta energy term was plotted against the calculated distance of the ligand ion (copper in plastocyanin and a heme iron in cytochrome c_6) and the magnesium ions found in the P700 chlorophylls. Five representative structures were chosen that minimized both terms and the structures were compared as seen in Figures 7 and 8. In the models of plastocyanin docked to PSI, a common docking face and domain were seen in all five models which compared favorably with the predictions of Ford et al. (*65*). In the models using cytochrome c_6, at least two different docking motifs were seen which lacked a common docking face and orientation. Possible causes for this alignment failure may have resulted from several sources including: the exclusion of metal ions which may contribute to aligning electrostatic interactions during the protein-protein docking; the rigid docking preformed may not be able to capture structural changes that occur at the time of docking (*76*) to stabilize

In Applications of Molecular Modeling to Challenges in Clean Energy; Fitzgerald, G., et al.;
ACS Symposium Series; American Chemical Society: Washington, DC, 2013.

the bound complex, in which case flexible docking should be pursued; or driving forces in the diffusion controlled (*77*) docking of cytochrome c_6 with PSI may be sufficiently small that Rosetta was unable to correctly estimate their value.

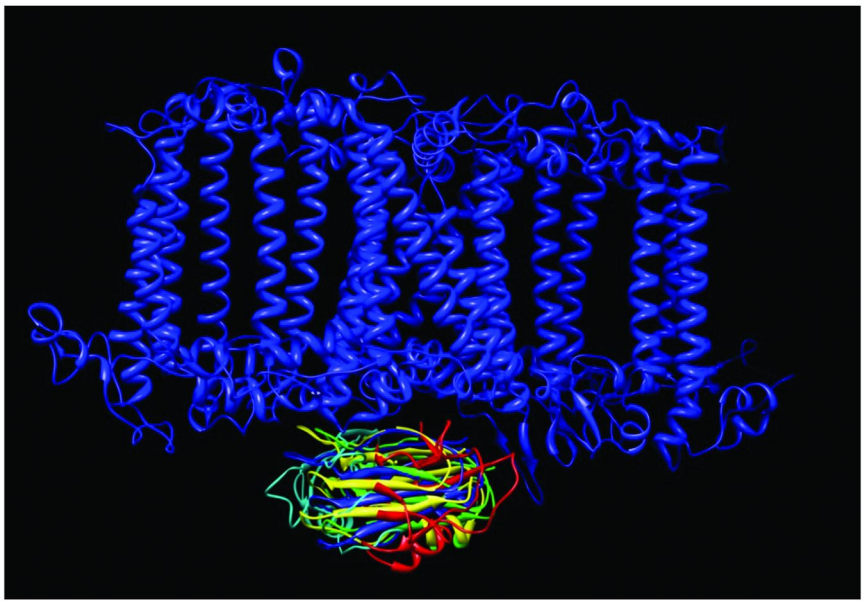

Figure 7. Combined structures showing docking convergence in the five most favorable docked PSI-plastocyanin Rosetta models.

To address the possible causes of failure in the rigid docking calculation of cytochrome c_6 to PSI, follow-up all-atom MD simulations of the docked complexes using the most favorable five Rosetta-docked structures as the initial starting trajectories were run. These MD simulations of the docked structures were completed using the AMBER modeling suite and Best phi and psi adjustment of the ff99SBildn force field as described earlier. Heme parameters were taken from the contributions of Bayly and Case which are distributed with the AMBER modeling suite (*36*). Copper bond, angle, and dihedral parameters were taken from Ross Walker's tutorial using poplar plastocyanin. After 80 ns of production MD, large differences were seen between the plastocyanin and cytochrome c_6 docking trajectories. MD simulations of the docked plastocyanin-PSI complex showed little structural fluctuations and varied minimally from the starting coordinates. Cytochrome c_6, on the other hand, was seen to traverse nearly the entire luminal surface of the PSI complex. While all the plastocyanin docking trajectories maintained the original PSI contacts, rotations in cytochrome c_6 molecules were evident with three of the five docking trajectories adopting a common docking orientation following the MD time course. Rotation of the

In Applications of Molecular Modeling to Challenges in Clean Energy; Fitzgerald, G., et al.;
ACS Symposium Series; American Chemical Society: Washington, DC, 2013.

cytochrome c_6 molecules to the common orientation was seen in two (of the three) instances to occur in proximity to the PsaF domain which may play a role in orienting cytochrome c_6 prior to docking and electron transfer. Further studies will be necessary to confirm this observation.

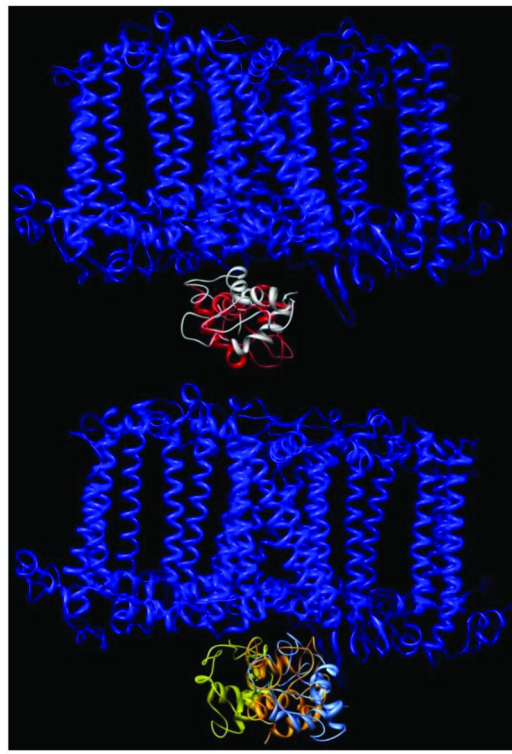

Figure 8. Rosetta docked models showing orientation and faces of the most favorable PSI-cytochrome c_6 structures. Clustering of the docked structures suggest at least two different motifs among the predicted complexes.

PSI Surface Interactions

Computational Approaches

Optimization of the interface between PSI and inorganic surfaces is necessary for the effective electron transfer between the surface and biomolecule. For instance, attachment of PSI to gold nanoparticles and unmodified gold electrodes has produced photosensitive and photoreactive systems (*78*, *79*); however this direct attachment to the gold surface can lead to protein denaturation and block access to active sites. The use of self-assembled monolayers (SAMs) to enhance binding and stability of PSI, as well as control its orientation on the electrode has been shown in the literature (*80*, *81*), however with limited fundamental understanding of the PSI/SAM interaction. Therefore, a comprehensive study of the surface assembly of PSI on various SAM modified electrodes was proposed

In Applications of Molecular Modeling to Challenges in Clean Energy; Fitzgerald, G., et al.;
ACS Symposium Series; American Chemical Society: Washington, DC, 2013.

utilizing experimental and computational approaches to characterize the surface of PSI and to optimize SAM candidates. Computational surface characterization was focused on polarity, luminal surface electrostatic potential, and luminal surface hydropathicity.

Our previous analysis of the PSI complex structure showed a very strong dipole oriented at slight tilt from the complex central axis, which may possibly contribute to orientation of the complex stromal- or luminal-side down during deposition on a surface (*82*). The Kyte-Doolittle representation of the hydropathicity of the photosystem I monomer (1JB0) shows distinct segregation of hydrophobic residues (red) to the interior and external, bilayer-exposed sides of the complex (Figure 9). Hydrophilic residues (blue) congregate to both stromal and luminal faces consistent with aqueous exposure. Notably, distribution of the luminal hydrophobic residues (in red) is uniform across the plane.

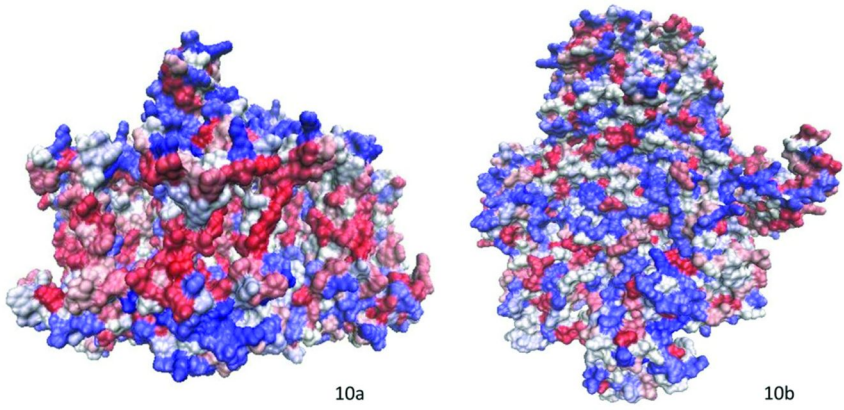

Figure 9. Hydropathicity analysis (Kyte-Doolittle algorithm) of side (10a) and luminal surfaces (10b) of photosystem I.

When the surfaces are remapped according to residue type, most of the hydrophilic luminal regions are shown to be composed of polar, non-charged residues (see Figure 10). The P700 docking site can be found near the center of luminal face, composed of a hydrophobic pocket surrounded by distinct positive and negative regions which is consistent with predicted long-range electrostatic steering of plastocyanin to the P700 binding site (*83*). Upon complex formation, short range hydrophobic and dipole-dipole interactions guide and ensure the optimal configuration of the mediator prior to electron transfer (*83*, *84*).

From these surface mapping studies, some characteristics for a luminal bound probe or SAM were made and later tested. The luminal surface of PSI is highly polar suggesting the favorability of a charged or polar probe. The calculated dipole traverses the stromal hump showing a vector moving away from the luminal face which indicates that a negative charge would be preferred over a positive SAM. The fairly homogenous distribution of hydrophobic and hydrophilic regions along the luminal surface may indicate the benefits of an amphiphilic molecule.

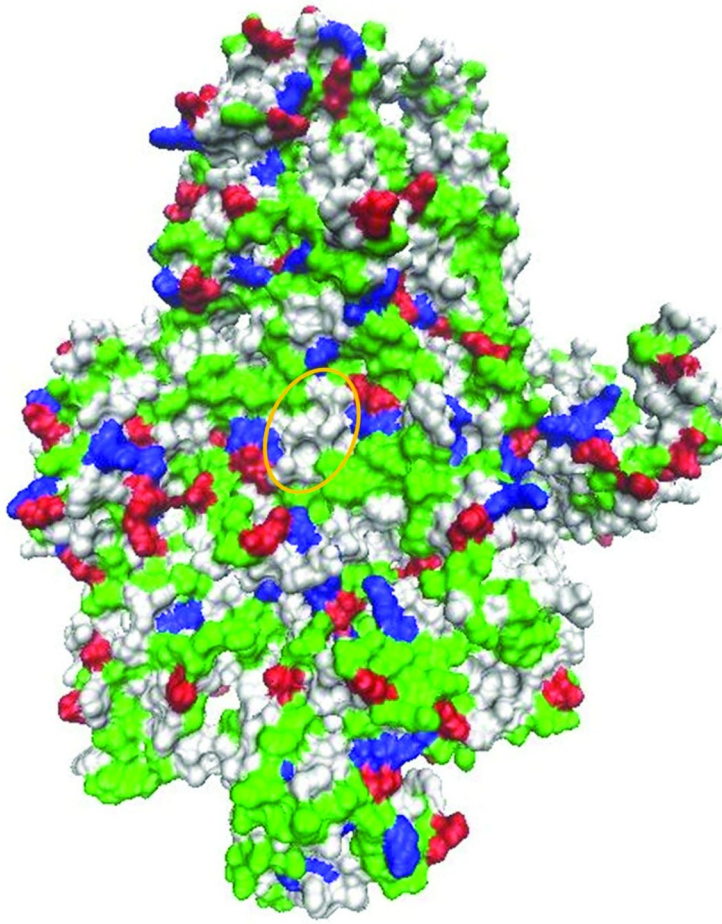

Figure 10. Luminal surface mapping of the PSI published structure (1JB0) by residue type. Acidic residues are shown in red, basic in blue, polar in green, and nonpolar in white. The P700 docking site is indicated by a yellow ellipsoid.

Experimental Results

In order to understand the dynamic effect of PSI surface functionalities in non-native environments, experimental surface assembly studies were performed on modified surfaces. Alkanethiol self assembled monolayers (SAMs) on gold substrates were chosen for the surface modifications in this work because of their facile fabrication, high reproducibility and easy of tailoring exposed functional groups. SAMs were composed of six-carbon length alkanethiol chains with varied terminal functional groups; amine (aminohexanethiol, AHT), methyl (hexanethiol, HT), alcohol (mercaptohexanol, MHO) and carboxylic acid (mercaptohexanoic acid, MHA).

In Applications of Molecular Modeling to Challenges in Clean Energy; Fitzgerald, G., et al.;
ACS Symposium Series; American Chemical Society: Washington, DC, 2013.

Gold substrates were formed via E-beam evaporation of gold on Silicon wafers (3000Å with 300Å Ti binding layer), followed by gold island flattening by intermittent flaming. SAMs were formed on Au electrodes by three day assembly in 1mM thiol ethanolic solution. The SAMs were rinsed with ethanol, and dried with nitrogen gas. PSI assembly on the SAMs was conducted via 90 minute adsorption at 4°C in the dark. After adsorption, all samples were rinsed with deionized water, and dried with nitrogen gas.

Experimental analysis of PSI surface assembly via Atomic Force Microscopy (AFM) showed that PSI assembled in higher density to hydrophilic surfaces. The hydrophobic SAM, hexanethiol (HT), showed negligible PSI assembly, with some PSI adherence at the gold island edge sites (Figure 11a). In contrast, aminohexanethiol (AHT) showed high PSI binding with approximately 621 PSI/μm^2. Similarly, mercaptohexanol (MHO) and mercaptohexanoic acid (MHA), negatively charged hydrophilic surfaces, showed similar densities of PSI; 626 and 502 PSI/μm^2 respectively.

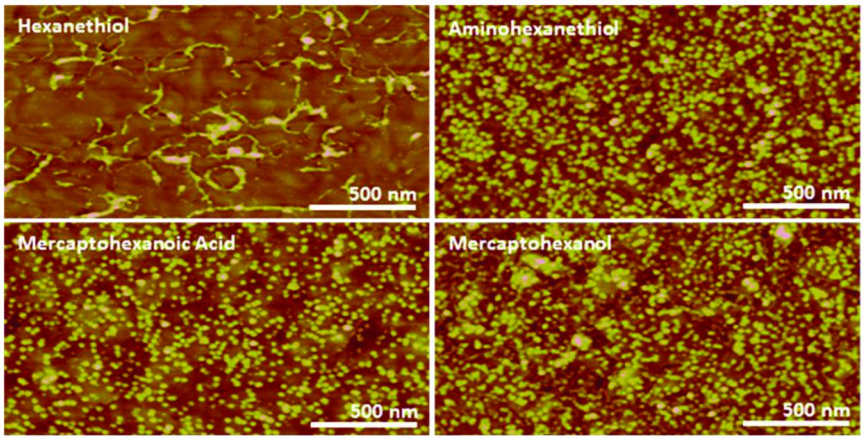

Figure 11. AFM images of PSI adsorption on (a) hexanethiol, (b) aminohexanethiol, (c) mercaptohexanoic acid, and (d) mercaptohexanol SAMs.

In agreement with the computational based predictions, hydrophilic SAMs were more effective than their hydrophobic complement, however the predictions of charge preference are more complex. Hydroxyl (MHO) and amine terminated (AHT) SAMs show similar PSI adherence rates with a slight improvement for the electronegative reactive groups (in agreement with predictions).

Mercaptohexananoic acid which is more electronegative than MHO showed a decrease in PSI binding suggesting that charged (or highly polar) probes may experience electrostatic repulsion from the PSI surface. Due to the limitations of available SAM head groups we were unable to test the effects of amphilicity on PSI adherence but intend to address those questions in future studies.

In Applications of Molecular Modeling to Challenges in Clean Energy; Fitzgerald, G., et al.;
ACS Symposium Series; American Chemical Society: Washington, DC, 2013.

Conclusions

Computational approaches are used to model the photosystem I complex and its interactions with biological electron carriers which can be used predict improvement with electrochemistry components. Long term all-atom simulations of PSI reveal contraction of solvent exposed protein domains and repacking of α-chorophyll antennae molecules. These changes were especially prevalent with the PsaL protein chain and chlorophylls CL1 1601, CL1 1217, CL1 1302, and CL1 1303. Many of these structural changes can be attributed to differences in simulation and crystallization solutions and suggest the need of lipid molecules or bilayer embedding for improved long-term simulation. Additionally, loss of secondary structure in our initial PSI molecular dynamics model, principally within the stromal hump, expose limitations in current iron-sulfur cluster parameterization approaches and demonstrate the need to include full amino acid ligands in the charge calculation. Structure and distance comparison of electron transfer branches show similarity to published structure with a decrease in B branch electron transfer distances. Early quantum analysis of ionization potential and orbital energies of the P700 chlorophylls from this model, the published X-ray structure and the Canfield ONIOM-optimized model show a consistent ionization potential and orbital energies with reasonable agreement.

Docking studies performed with established algorithms and subsequent all-atom MD simulations suggest a difference between plastocyanin and cytochrome c_6 docking and interaction with the PSI luminal surface. In particular cytochrome c_6 was found to traverse and sample much of the PSI luminal surface while plastocyanin forms a more static interaction at the P700 site. In addition, PsaF may play a role in orientation correction of cytochrome c_6 at the luminal surface in cyanobacteria.

Computational PSI luminal surface characterization and dipole calculations were used to improve design of surface-assembly molecules (SAM). It was shown that SAM probes that were hydrophilic and electronegative demonstrated best PSI attachment to gold-plated electrodes; however, experimental verification indicated that highly electronegative or ionic head groups may actually decrease PSI counts.

Acknowledgments

We gratefully acknowledge financial support from the U. S. Department of the Army and U.S. Army Materiel Command. Research was supported in part by a contractual appointment to the U.S. Army Research Laboratory Postdoctoral Fellowship Program administered by the Oak Ridge Associated Universities. We would also like to thank the Department of Defense High Performance Computing (DOD HPC) modernization program and CCAC for computer resources and support without which this work would not be possible.

References

1. Palsson, L. O.; Flemming, C.; Gobets, B.; van Grondelle, R.; Dekker, J. P.; Schlodder, E. Energy transfer and charge separation in photosystem I:

P700 oxidation upon selective excitation of the long-wavelength antenna chlorophylls of *Synechococcus elongatus*. *Biophys. J.* **1998**, *74* (5), 2611–2622.
2. Blankenship, R. E.; Tiede, D. M.; Barber, J.; Brudvig, G. W.; Fleming, G.; Ghirardi, M.; Gunner, M. R.; Junge, W.; Kramer, D. M.; Melis, A.; Moore, T. A.; Moser, C. C.; Nocera, D. G.; Nozik, A. J.; Ort, D. R.; Parson, W. W.; Prince, R. C.; Sayre, R. T. Comparing photosynthetic and photovoltaic efficiencies and recognizing the potential for improvement. *Science* **2011**, *332*, 805–809.
3. Ghirardi, M. L.; Zhang, L.; Lee, J. W.; Flynn, T.; Seibert, M.; Greenbaum, E.; Melis, A. Microalgae: A green source of renewable H_2. *Trends Biotechnol.* **2000**, *18* (12), 506–511.
4. Ghirardi, M. L.; Posewitz, M. C.; Maness, P. C.; Dubini, A.; Yu, J.; Seibert, M. Hydrogenases and hydrogen photoproduction in oxygenic photosynthetic organisms. *Annu. Rev. Plant Biol.* **2007**, *58*, 71–91.
5. Healey, F. Hydrogen evolution by several algae. *Planta* **1970**, *91* (3), 220–226.
6. Stuart, T. S.; Kaltwasser, H. Photoproduction of hydrogen by photosystem I of *Scenedesmus*. *Planta* **1970**, *91* (4), 302–313.
7. Winkler, M.; Hemschemeier, A.; Gotor, C.; Melis, A.; Happe, T. [Fe]-hydrogenases in green algae: Photo-fermentation and hydrogen evolution under sulfur deprivation. *Int. J. Hydrogen Energy* **2002**, *27* (11), 1431–1439.
8. Rupprecht, J. From systems biology to fuel: *Chlamydomonas reinhardtii* as a model for a systems biology approach to improve biohydrogen production. *J. Biotechnol.* **2009**, *142* (1), 10–20.
9. Hemschemeier, A.; Fouchard, S.; Cournac, L.; Peltier, G.; Happe, T. Hydrogen production by *Chlamydomonas reinhardtii*: An elaborate interplay of electron sources and sinks. *Planta* **2008**, *227* (2), 397–407.
10. Melis, A.; Zhang, L.; Forestier, M.; Ghirardi, M. L.; Seibert, M. Sustained photobiological hydrogen gas production upon reversible inactivation of oxygen evolution in the green alga *Chlamydomonas reinhardtii*. *Plant Physiol.* **2000**, *122* (1), 127–136.
11. Ihara, M.; Nakamoto, H.; Kamachi, T.; Okura, I.; Maedal, M. Photoinduced hydrogen production by direct electron transfer from photosystem I cross-linked with cytochrome c3 to [NiFe]-hydrogenase. *Photochem. Photobiol.* **2006**, *82* (6), 1677–1685.
12. Ihara, M.; Nishihara, H.; Yoon, K. S.; Lenz, O.; Friedrich, B.; Nakamoto, H.; Kojima, K.; Honma, D.; Kamachi, T.; Okura, I. Light-driven hydrogen production by a hybrid complex of a [NiFe]-hydrogenase and the cyanobacterial photosystem I. *Photochem. Photobiol.* **2007**, *82* (3), 676–682.
13. McTavish, H. Hydrogen evolution by direct electron transfer from photosystem I to hydrogenases. *J. Biochem.* **1998**, *123* (4), 644–649.
14. Lubner, C. E.; Knörzer, P.; Silva, P. J. N.; Vincent, K. A.; Happe, T.; Bryant, D. A.; Golbeck, J. H. Wiring an [FeFe]-hydrogenase with photosystem I for light-induced hydrogen production. *Biochemistry* **2010**, *49* (48), 10264–10266.

15. Schwarze, A.; Kopczak, M. J.; Rögner, M.; Lenz, O. Requirements for construction of a functional hybrid complex of photosystem I and [NiFe]-hydrogenase. *Appl. Environ. Microbiol.* **2010**, *76* (8), 2641–2651.
16. Qian, D. J.; Liu, A. R.; Nakamura, C.; Wenk, S. O.; Miyake, J. Photoinduced hydrogen evolution in an artificial system containing photosystem I, hydrogenase, methyl viologen and mercaptoacetic acid. *Chin. Chem. Lett.* **2008**, *19* (5), 607–610.
17. Millsaps, J. F.; Bruce, B. D.; Lee, J. W.; Greenbaum, E. Nanoscale photosynthesis: Photocatalytic production of hydrogen by platinized photosystem I reaction centers. *Photochem. Photobiol.* **2001**, *73* (6), 630–635.
18. Lubner, C. E.; Grimme, R.; Bryant, D. A.; Golbeck, J. H. Wiring photosystem I for direct solar hydrogen production. *Biochemistry* **2009**, *49* (3), 404–414.
19. Jordan, P.; Fromme, P.; Witt, H. T.; Klukas, O.; Saenger, W.; Kraub, N. Three-dimensional structure of cyanobacterial photosystem I at 2.5 A resolution. *Nature* **2001**, *411*, 909–917.
20. Byrdin, M.; Jordan, P.; Krauss, N.; Fromme, P.; Stehlik, D.; Schlodder, E. Light harvesting in photosystem I: Modeling based on the 2.5-Å structure of photosystem I from *Synechococcus elongatus*. *Biophys. J.* **2002**, *83* (1), 433–457.
21. Sener, M. K.; Lu, D.; Ritz, T.; Park, S.; Fromme, P.; Schulten, K. Robustness and optimality of light harvesting in cyanobacterial photosystem I. *J. Phys. Chem B* **2002**, *106* (32), 7948–7960.
22. Yang, M.; Damjanović, A.; Vaswani, H. M.; Fleming, G. R. Energy transfer in photosystem I of cyanobacteria *Synechococcus elongatus*: Model study with structure-based semi-empirical hamiltonian and experimental spectral density. *Biophys. J.* **2003**, *85* (1), 140–158.
23. Ivashin, N.; Larsson, S. Electron transfer pathways in photosystem I reaction centers. *Chem. Phys. Lett.* **2003**, *375* (3), 383–387.
24. Adolphs, J.; Müh, F.; Madjet, M. E. A.; Busch, M. S.; Renger, T. Structure-based calculations of optical spectra of photosystem I suggest an asymmetric light-harvesting process. *J. Am. Chem. Soc.* **2010**, *132* (10), 3331–3343.
25. Ishikita, H.; Knapp, E. W. Redox potential of quinones in both electron transfer branches of photosystem I. *J. Biol. Chem.* **2003**, *278* (52), 52002–52011.
26. Ptushenko, V. V.; Cherepanov, D. A.; Krishtalik, L. I.; Semenov, A. Y. Semi-continuum electrostatic calculations of redox potentials in photosystem I. *Photosynth. Res.* **2008**, *97* (1), 55–74.
27. Sun, Y.; Dai, Z.; Wang, W.; Sun, Y. A TDDFT study on the excitation of P700. *Chem. Phys. Lett.* **2007**, *434* (1), 111–115.
28. Plato, M.; Krauß, N.; Fromme, P.; Lubitz, W. Molecular orbital study of the primary electron donor P700 of photosystem I based on a recent X-ray single crystal structure analysis. *Chem. Phys.* **2003**, *294* (3), 483–499.
29. Lin, T. J.; O'Malley, P. J. Binding site influence on the electronic structure and electron paramagnetic resonance properties of the phyllosemiquinone free radical of photosystem I. *J. Phys. Chem. B* **2011**, *115* (29), 9311–9319.

30. Canfield, P.; Dahlbom, M. G.; Hush, N. S.; Reimers, J. R. Density-functional geometry optimization of the 150 000-atom photosystem-I trimer. *J. Chem. Phys.* **2006**, *124*, 024301.
31. Yin, S.; Dahlbom, M. G.; Canfield, P. J.; Hush, N. S.; Kobayashi, R.; Reimers, J. R. Assignment of the Q y absorption spectrum of photosystem-I from *Thermosynechococcus elongatus* based on CAM-B3LYP calculations at the PW91-optimized protein structure. *J. Phys. Chem. B* **2007**, *111* (33), 9923–9930.
32. Myshkin, E.; Leontis, N. B.; Bullerjahn, G. S. Computational simulation of the docking of *Prochlorothrix hollandica* plastocyanin to photosystem I: Modeling the electron transfer complex. *Biophys. J.* **2002**, *82* (6), 3305–3313.
33. Jolley, C. C.; Wells, S. A.; Hespenheide, B. M.; Thorpe, M. F.; Fromme, P. Docking of photosystem I subunit C using a constrained geometric simulation. *J. Am. Chem. Soc.* **2006**, *128* (27), 8803–8812.
34. Farah, J.; Rappaport, F.; Choquet, Y.; Joliot, P.; Rochaix, J. Isolation of a psaF-deficient mutant of Chlamydomonas reinhardtii: Efficient interaction of plastocyanin with the photosystem I reaction center is mediated by the PsaF subunit. *EMBO J.* **1995**, *14* (20), 4976.
35. Pigache, A.; Cieplak, P.; Dupradeau, F. In *Automatic and Highly Reproducible RESP and ESP Charge Derivation: Application to the Development of Programs RED and X RED*, 227th ACS National Meeting, Anaheim, CA, 2004.
36. Case, D. A.; Cheatham, T. E.; Darden, T.; Gohlke, H.; Luo, R.; Merz, K. M.; Onufriev, A.; Simmerling, C.; Wang, B.; Woods, R. J. The Amber biomolecular simulation programs. *J. Comput. Chem.* **2005**, *26* (16), 1668–1688.
37. Torres, R. A.; Lovell, T.; Noodleman, L.; David, A. Density functional and reduction potential calculations of Fe4S4 clusters. *J. Am. Chem. Soc.* **2003**, *125* (7), 1923–1936.
38. Bayly, C. I.; Cieplak, P.; Cornell, W. D.; Kollman, P. A. A well-behaved electrostatic potential based method using charge restraints for deriving atomic charges: The RESP model. *J. Phys. Chem.* **1993**, *97*, 10269–10280.
39. Wang, J.; Wolf, R. M.; Caldwell, J. W.; Kollman, P. A.; Case, D. A. Development and testing of a general amber force field. *J. Comput. Chem.* **2004**, *25* (9), 1157–1174.
40. Lindorff-Larsen, K.; Piana, S.; Palmo, K.; Maragakis, P.; Klepeis, J. L.; Dror, R. O.; Shaw, D. E. Improved side-chain torsion potentials for the Amber ff99SB protein force field. *Proteins: Struct., Funct., Bioinf.* **2010**, *78* (8), 1950–1958.
41. Best, R. B.; Hummer, G. Optimized molecular dynamics force fields applied to the helix−coil transition of polypeptides. *The J. Phys. Chem. B* **2009**, *113* (26), 9004–9015.
42. Joung, I. S.; Cheatham, T. E., III Determination of alkali and halide monovalent ion parameters for use in explicitly solvated biomolecular simulations. *The J. Phys. Chem. B* **2008**, *112* (30), 9020–9041.

43. Pendley, S. S.; Yu, Y. B.; Cheatham, T. E. Molecular dynamics guided study of salt bridge length dependence in both fluorinated and non-fluorinated parallel dimeric coiled-coils. *Proteins: Struct., Funct., Bioinf.* **2008**, *74* (3), 612–629.
44. Guergova-Kuras, M.; Boudreaux, B.; Joliot, A.; Joliot, P.; Redding, K. Evidence for two active branches for electron transfer in photosystem I. *Pro. Natl. Acad. Sci.* **2001**, *98* (8), 4437–4442.
45. Joliot, P.; Joliot, A. In vivo analysis of the electron transfer within Photosystem I: Are the two phylloquinones involved? *Biochemistry* **1999**, *38* (34), 11130–11136.
46. Xu, W.; Chitnis, P.; Valieva, A.; van der Est, A.; Brettel, K.; Guergova-Kuras, M.; Pushkar, J.; Zech, S. G.; Stehlik, D.; Shen, G. Electron transfer in cyanobacterial photosystem I. II. Determination of forward electron transfer rates of site-directed mutants in a putative electron transfer pathway from A0 through A1 to FX. *J. Biol. Chem.* **2003**, *270* (30), 27876–27887.
47. Karyagina, I.; Pushkar, Y.; Stehlik, D.; van der Est, A.; Ishikita, H.; Knapp, E.-W.; Jagannathan, B.; Agalarov, R.; Golbeck, J. H. Contributions of the protein environment to the midpoint potentials of the A1 phylloquinones and the Fx iron-sulfur cluster in photosystem I. *Biochemistry* **2007**, *46*, 10804–10816.
48. Bittl, R.; Zech, S. G.; Fromme, P.; Witt, H. T.; Lubitz, W. Pulsed EPR structure analysis of photosystem I single crystals: Localization of the phylloquinone acceptor. *Biochemistry* **1997**, *36*, 12001–12004.
49. Parusel, A. B. J.; Grimme, S. A theoretical study of the excited states of chlorophyll a and pheophytin a. *J. Phys. Chem. B* **2000**, *104* (22), 5395–5398.
50. Suendo, V.; Viridi, S. Ab initio calculation of UV-Vis absorption spectra of a single molecule chlorophyll a: Comparison study between RHF/CIS, TDDFT, and semi-empirical methods. *ITB J. Sci.* **2012**, *44A* (2), 93–112.
51. Saito, K.; Ishikita, H. Cationic state distribution over the P700 chlorophyll pair in photosystem I. *Biophys. J.* **2011**, *101* (8), 2018–2025.
52. Gunner, M. Computational analysis of photosynthetic systems. *Photosynth. Res.* **2008**, *97* (1), 1–3.
53. Dreuw, A.; Harbach, P. H. P.; Mewes, J. M.; Wormit, M. Quantum chemical excited state calculations on pigment–protein complexes require thorough geometry re-optimization of experimental crystal structures. *Theor. Chem. Acc.* **2010**, *125* (3), 419–426.
54. Sinnecker, S.; Koch, W.; Lubitz, W. Chlorophyll a radical ions: A density functional study. *J. Phys. Chem. B* **2002**, *106* (20), 5281–5288.
55. Takahashi, R.; Hasegawa, K.; Noguchi, T. Effect of charge distribution over a chlorophyll dimer on the redox potential of P680 in photosystem II as studied by density functional theory calculations. *Biochemistry* **2008**, *47* (24), 6289–6291.
56. Ishikita, H.; Saenger, W.; Biesiadka, J.; Loll, B.; Knapp, E. W. How photosynthetic reaction centers control oxidation power in chlorophyll pairs P680, P700, and P870. *Proc. Natl. Acad. Sci.* **2006**, *103* (26), 9855–9860.

57. Webber, A. N.; Lubitz, W. P700: The primary electron donor of photosystem I. *Biochim. Biophys. Acta, Bioenerg.* **2001**, *1507* (1), 61–79.
58. Hasegawa, J.; Ozeki, Y.; Ohkawa, K.; Hada, M.; Nakatsuji, H. Theoretical study of the excited states of chlorin, bacteriochlorin, pheophytin a, and chlorophyll a by the SAC/SAC-CI method. *J. Phys. Chem. B* **1998**, *102* (7), 1320–1326.
59. Vokáčová, Z.; Burda, J. V. Computational study on spectral properties of the selected pigments from various photosystems: Structure−transition energy relationship. *J. Phys. Chem. A* **2007**, *111* (26), 5864–5878.
60. Kim, S.; Sackstedert, C. A.; Bixby, K. A.; Barry, B. A. A reaction-induced FTIR study of cyanobacterial photosystem I. *Biochemistry* **2001**, *40*, 15384–15395.
61. Breton, J.; Nabedryk, E.; Leibl, W. FTIR study of the primary electron Donor of photosystem I (P700) revealing delocalization of the charge in P700+ and localization of the triplet character in 3P700. *Biochemistry* **1999**, *38*, 11587–11593.
62. Bender, S. L.; Keough, J. M.; Boesch, S. E.; Wheeler, R. A.; Barry, B. A. The vibrational spectrum of the secondary electron acceptor, A1, in photosystem I. *J. Phys. Chem. B* **2008**, *112*, 3844–3852.
63. Niklas, J.; Epel, B.; Antonkine, M. L.; Sinnecker, S.; Pandelia, M.-E.; Lubitz, W. Electronic structure of the quinone radical anion $A_1^{\bullet-}$ of photosystem I investigated by advanced pulse EPR and ENDOR techniques. *J. Phys. Chem. B* **2009**, *113*, 10367–10379.
64. Lubitz, W. EPR Studies of the Primary Electron Donor P700 in Photosystem I. In *Photosystem I. The Light-Driven Plastocyanin: Ferredoxin Oxidoreductase*; Goldbeck, J. H., Ed.; Springer: Dortrecht, 2006; Vol. 24, pp 245−269.
65. Ruffle, S. V.; Mustafa, A. O.; Kitmitto, A.; Holzenburg, A.; Ford, R. C. The location of plastocyanin in vascular plant photosystem I. *J. Biol. Chem.* **2002**, *277* (28), 25692.
66. Sommer, F.; Drepper, F.; Hippler, M. The luminal helix of PsaB is essential for recognition of plastocyanin or cytochrome c6 and fast electron transfer to photosystem I in Chlamydomonas reinhardtii. *J. Biol. Chem.* **2002**, *227* (8), 6573–6581.
67. Frazao, C.; Soares, C.; Carrondo, M.; Pohl, E.; Dauter, Z.; Wilson, K.; Herves, M.; Navarro, J.; De la Rosa, M.; Sheldrick, G. Ab initio determination of the crystal structure of cytochrome c6 and comparison with plastocyanin. *Structure* **1995**, *3* (11), 1159–1169.
68. Molina-Heredia, F. P.; Diaz-Quintana, A.; Hervas, M.; Navarro, J. A.; De la Rosa, M. A. Site-directed mutagenesis of cytochrome c6 from Anabaena species PCC 7119. Identification of surface residues of the heme protein involved in photosystem I reduction. *J. Biol. Chem.* **1999**, *274* (47), 33565–33570.
69. Bertini, I.; Bryant, D. A.; Ciurli, S.; Dikiy, A.; Fernández, C. O.; Luchinat, C.; Safarov, N.; Vila, A. J.; Zhao, J. Backbone dynamics of plastocyanin in both oxidation states: Solution structure of the reduced form and comparison with the oxidized state. *J. Biol. Chem.* **2001**, *276* (50), 47217–47226.

70. Beißinger, M.; Sticht, H.; Sutter, M.; Ejchart, A.; Haehnel, W.; Rösch, P. Solution structure of cytochrome c6 from the thermophilic cyanobacterium *Synechococcus elongatus*. *The EMBO J.* **1998**, *17* (1), 27–36.
71. De Vries, S. J.; Van Dijk, M.; Bonvin, A. M. J. J. The HADDOCK web server for data-driven biomolecular docking. *Nat. Protoc.* **2010**, *5* (5), 883–897.
72. Comeau, S. R.; Gatchell, D. W.; Vajda, S.; Camacho, C. J. ClusPro: An automated docking and discrimination method for the prediction of protein complexes. *Bioinformatics* **2004**, *20* (1), 45–50.
73. Tovchigrechko, A.; Vakser, I. A. GRAMM-X public web server for protein–protein docking. *Nucleic Acids Res.* **2006**, *34* (suppl 2), W310–W314.
74. Lyskov, S.; Gray, J. J. The RosettaDock server for local protein–protein docking. *Nucleic Acids Res.* **2008**, *36* (suppl 2), W233–W238.
75. Chaudhury, S.; Lyskov, S.; Gray, J. J. PyRosetta: A script-based interface for implementing molecular modeling algorithms using Rosetta. *Bioinformatics* **2010**, *26* (5), 689.
76. Diaz-Moreno, I.; Diaz-Quintana, A.; Molina-Heredia, F. P.; Nieto, P. M.; Hansson, O.; De la Rosa, M. A.; Karlsson, B. G. NMR analysis of the transient complex between membrane photosystem I and soluble cytochrome c6. *J. Biol. Chem.* **2005**, *280* (9), 7925.
77. Fromme, P.; Melkozernov, A.; Jordan, P.; Krauss, N. Structure and function of photosystem I: Interaction with its soluble electron carriers and external antenna systems. *FEBS Lett.* **2003**, *555* (1), 40–44.
78. Lee, I.; Lee, J. W.; Stubna, A.; Greenbaum, E. Measurement of electrostatic potentials above oriented single photosynthetic reaction centers. *J. Phys. Chem. B* **2000**, *104* (11), 2439–2443.
79. Ciesielski, P. N.; Scott, A. M.; Faulkner, C. J.; Berron, B. J.; Cliffel, D. E.; Jennings, G. K. Functionalized nanoporous gold leaf electrode films for the immobilization of photosystem I. *ACS Nano* **2008**, *2* (12), 2465–2472.
80. Faulkner, C. J.; Lees, S.; Ciesielski, P. N.; Cliffel, D. E.; Jennings, G. K. Rapid assembly of photosystem I monolayers on gold electrodes. *Langmuir* **2008**, *24* (16), 8409–8412.
81. Yan, X.; Faulkner, C.; Jennings, G. K.; Cliffel, D. E. Photosystem I in Langmuir−Blodgett and Langmuir−Schaefer monolayers. *Langmuir* **2012**, *28* (42), 15080–15086.
82. Manocchi, A. K.; Baker, D. R.; Pendley, S. S.; Hurley, M. M.; Bruce, B. D.; Sumner, J. J.; Lundgren, C. A. Photocurrent generation from surface assembled photosystem I on alkanethiol modified electrodes. *Langmuir* **2012**, *29* (7), 2412–2419.
83. Hope, A. Electron transfers amongst cytochrome *f*, plastocyanin and photosystem I: Kinetics and mechanisms. *Biochim. Biophys. Acta, Bioenerg.* **2000**, *1456* (1), 5–26.
84. Hippler, M.; Reichert, J.; Sutter, M.; Zak, E.; Altschmied, L.; Schröer, U.; Herrmann, R.; Haehnel, W. The plastocyanin binding domain of photosystem I. *EMBO J.* **1996**, *15* (23), 6374.

NO. OF
COPIES ORGANIZATION

1 (PDF) DEFENSE TECHNICAL INFORMATION CTR DTIC OCA

1 (PDF) DIRECTOR US ARMY RESEARCH LAB IMAL HRA

1 (PDF) DIRECTOR US ARMY RESEARCH LAB RDRL CIO LL

1 (PDF) GOVT PRINTG OFC A MALHOTRA

ABERDEEN PROVING GROUND

1 (PDF) DIR USARL RDRL WML B M HURLEY

INTENTIONALLY LEFT BLANK.